Modelling of the ICRF induced $E \times B$ convection in the scrape-off-layer of ASDEX Upgrade

2016 Plasma Phys. Control. Fusion 58 095005

(http://iopscience.iop.org/0741-3335/58/9/095005)

IOP Publishing Plasma Physics and Controlled Fusion

Plasma Phys. Control. Fusion **58** (2016) 095005 (12pp) doi:10.1088/0741-3335/58/9/095005

Modelling of the ICRF induced $E \times B$ convection in the scrape-off-layer of ASDEX Upgrade

W Zhang[1,2,3], Y Feng[2], J-M Noterdaeme[1,2], V Bobkov[2], L Colas[4], D Coster[2], T Lunt[2], R Bilato[2], J Jacquot[2], R Ochoukov[2], D Van Eester[5], A Křivská[5], P Jacquet[6], L Guimarais[7] and the ASDEX Upgrade Team[2]

[1] Applied Physics Department, University of Ghent, Ghent, Belgium
[2] Max-Planck-Institut für Plasmaphysik, Garching/Greifswald, Germany
[3] Institute of Plasma Physics, Chinese Academy of Sciences, Hefei, People's Republic of China
[4] CEA, IRFM, F-13108 Saint-Paul-Lez-Durance, France
[5] Laboratory for Plasma Physics, ERM/KMS, Brussels, Belgium
[6] CCFE, Culham Science Centre, Abingdon, UK
[7] Instituto de Plasmas e Fusão Nuclear, IST, Universidade de Lisboa, Lisbon, Portugal

E-mail: wei.zhang@ipp.mpg.de

Received 20 April 2016, revised 20 June 2016
Accepted for publication 29 June 2016
Published 19 August 2016

Abstract

In magnetic controlled fusion devices, plasma heating with radio-frequency (RF) waves in the ion cyclotron (IC) range of frequency relies on the electric field of the fast wave to heat the plasma. However, the slow wave can be generated parasitically. The electric field of the slow wave can induce large biased plasma potential (DC potential) through sheath rectification. The rapid variation of the rectified potential across the equilibrium magnetic field can cause significant convective transport ($E \times B$ drifts) in the scrape-off layer (SOL). In order to understand this phenomenon and reproduce the experiments, 3D realistic simulations are carried out with the 3D edge plasma fluid and kinetic neutral code EMC3-Eirene in ASDEX Upgrade. For this, we have added the prescribed drift terms to the EMC3 equations and verified the 3D code results against the analytical ones in cylindrical geometry. The edge plasma potential derived from the experiments is used to calculate the drift velocities, which are then treated as input fields in the code to obtain the final density distributions. Our simulation results are in good agreement with the experiments.

Keywords: $E \times B$ convection, RF sheath, SOL density, 3D simulation, radio-frequency heating

(Some figures may appear in colour only in the online journal)

1. Introduction

Plasma heating with radio-frequency waves in the ion cyclotron range of frequency (ICRF) is one of the main auxiliary plasma heating methods in tokamaks. It relies on the electric field of the fast wave to accelerate the charged particles which will then heat the plasma through collisions [1]. However, the slow wave can also be generated parasitically, either directly induced by the antenna fields (corresponding to the near-field sheath), or through mode conversion when the unabsorbed fast wave change polarization close to the wall (corresponding to the far-field sheath) [2, 3]. Due to the acceleration in the parallel electric field $E_{\|}$ of the slow wave (parallel to the equilibrium magnetic field), electrons are lost much faster to the wall than the heavier ions. In order to keep quasi-neutrality in the confined region, the plasma develops a potential that forms a large barrier and prevents more electrons from entering the sheath (sheath rectification). The time averaged ICRF rectified direct current (DC) sheath potential is in the range of several hundreds of volts, while the DC Bohm sheath

potential is only in the range of a few tens of volts. The relation between the RF rectified sheath potential (Φ_{RF}) and the DC Bohm sheath potential (Φ_B) can be described with the formula $\Phi_{RF} = C_{sh}V_{sh} + \Phi_B$ [4], in which C_{sh} is the 'rectification factor' and V_{sh} is the magnitude of the instantaneous (or RF) sheath voltage. The RF enhanced edge plasma potential Φ_{RF} has been observed in many tokamaks, such as ASDEX Upgrade (AUG) [5, 6], JET [7], EAST [8], Tore Supra [9] and Alcator C-Mod [10].

It should be noted that Φ_{RF} is nearly constant along the magnetic field in the confined plasma region and the large potential drop only happens within the sheath. This is because the parallel electric field in the confined region tends to be screened by the rapid motion of the electrons and the large parallel electron conductivity [11]. The ions entering into the sheath will gain an additional energy of $q\Phi_{sh}$, in which q is the charge number and Φ_{sh} is the potential drop in the sheath. In the presence of powered antenna, the ions accelerated in the sheath can be energetic enough to cause physical sputtering and self-sputtering [12], while the impurities thus generated can degrade the plasma performance. The energy lost in the sheath (i.e. sheath power dissipation) can reduce the ICRF heating efficiency [13].

Moreover, Φ_{RF} is inhomogeneous in the direction perpendicular to the equilibrium magnetic field. The rapid variation of Φ_{RF} across the magnetic field can generate significant $E \times B$ drifts (RF convection). The RF convection can not only modify the SOL density and affect the coupling of the ICRF power, but also enhance the strength of plasma-wall interactions by driving more plasma fluxes locally to the wall. For larger tokamaks such as ITER, such $E \times B$ convections can largely increase radial transport and drive local particle fluxes to the wall, as a result the intensity of heat load on the wall can be significantly enhanced. Thus it is critically important to investigate the edge plasma convection driven by the RF rectified sheath.

The influence of ICRF waves on the SOL and the plasma-wall interactions has long been an interesting topic [14, 15]. For instance, large efforts were devoted into understanding the RF sheath [16, 17], the RF induced edge plasma convection [11, 13, 18] and the associated impurity generations [13, 19–21]. The previous AUG experiments [6, 22] have shown that the RF rectified sheaths are responsible for much of the interactions between the ICRF and edge plasma. The important role of the RF convective cells and the associated pump-out effects can be confirmed through analyzing the poloidal variations of edge plasma density in experiments [13, 18]. It was indicated that the modified transport is responsible for the flattened profiles in the SOL and the increased plasma interaction with the antennas. In addition, RF convection was suspected to influence the edge transport barrier in H-modes and spread the power load on the divertor targets [11].

Numerical efforts have also been spent in investigating the RF convection. However the previous simulations involving the RF induced SOL density modifications are only 1D or 2D [11, 18, 23]. In our study we have carried out 3D simulations in realistic geometry with the 3D edge plasma fluid and kinetic neutral code EMC3-Eirene [24]. Note that drifts are not considered in the previous versions of the EMC3-Eirene code. In our study we have added the prescribed drift terms to the particle, momentum and energy transport equations in the EMC3 code. The corresponding discussions are given in section 2. To demonstrate that only 3D simulations are feasible for this study, field line tracings are made for three points $A0$, $B0$ and $C0$, as illustrated in figure 1. These three points are located in the same poloidal cross-section and same flux surface. Because Φ_{RF} is constant along the equilibrium magnetic field, thus $\Phi_{A0} = \Phi_{A1}, \Phi_{B0} = \Phi_{B1}, \Phi_{C0} = \Phi_{C1}$. If toroidal axisymmetry is assumed (thus 3D becomes 2D), then the potentials for different points in the same toroidal cross-section and same flux surface are the same, i.e. $\Phi_{A1} = \Phi_{B1} = \Phi_{C1}$. Subsequently one can get $\Phi_{A0} = \Phi_{B0} = \Phi_{C0}$, the potential becomes constant on the same flux surface in the SOL, i.e. $\Phi_{SOL} = \Phi(\psi)$. As a result, the potentials only vary in the radial direction and the 3D simulations become only 1D. Thus toroidal axisymmetry cannot be assumed in this study, and 2D codes such as B2-EIRENE or EDGE2D-EIRENE are not suitable for this work even if realistic geometries are considered. For correct and detailed descriptions of the convective cells and density modifications, 3D simulations in realistic simulations are necessary.

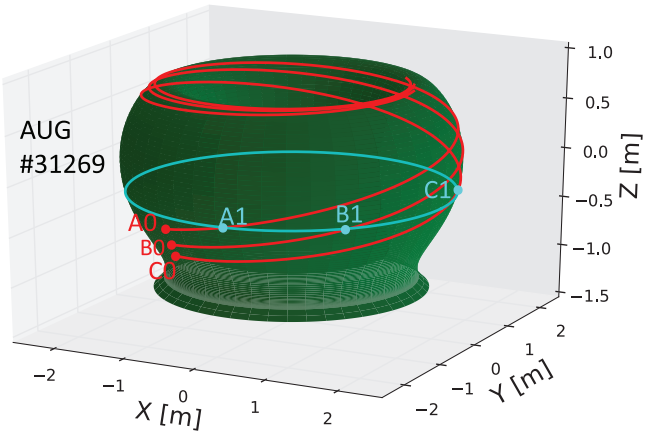

Figure 1. Field line tracings indicate a 3D code is necessary to include the 3D RF rectified sheath potential.

In addition to the RF convection, the ponderomotive force can also play an important role in reshaping the final density profiles [25, 26]. It is found that the ponderomotive effects are typically small for AUG L-mode plasma parameters and is not considered in this work. From our estimations, a coupling of 1MW ICRF power gives a $E_{\parallel}$ of ~30V cm^{-1} in front of the Faraday screen, and this results in a ponderomotive potential of only 8 V with $f_{ICRF} = 35$ MHz.

Our paper is organized as follows. In section 2, the prescribed drift terms in the EMC3 equations and their verification in the code are discussed. In section 3, experimental evidences of the SOL density modifications caused by the RF convection are presented. In section 4, 3D realistic simulations are carried out. These include the validations of the background plasmas, the 3D calculations of the potential and convective drifts, the simulations of the density modifications caused by the RF convection and the calculations of plasma fluxes to the wall. Finally conclusions and outlooks are given in section 5.

2. Prescribed drifts in EMC3-Eirene

EMC3-Eirene is now a widely used 3D code in magnetic controlled fusion community. It is not only a standard tool for stellarators, but also finds wide applications in tokamaks and linear machines [27]. EMC3 [24] solves a set of steady state Braginskii's equations for mass, parallel momentum, electron and ion energy, and is self-consistently coupled to Eirene code [28], which solves the Boltzmann equation for neutrals. The previous versions of EMC3-Eirene do not include drifts and volume recombination [24]. To account for $E \times B$ drifts, the EMC3 equations have been modified as follows and the new terms are indicated in bold:

$$\nabla \cdot \left(n_{\mathrm{i}} V_{\mathrm{i}\|} \vec{b} + \mathbf{n_i V_d \vec{b}_\perp} - D_{\mathrm{i}} \vec{b}_\perp \vec{b}_\perp \cdot \nabla n_{\mathrm{i}} \right) = S_{\mathrm{p}} \tag{1}$$

$$\nabla \cdot \Big(m_{\mathrm{i}} n_{\mathrm{i}} V_{\mathrm{i}\|} V_{\mathrm{i}\|} \vec{b} + \mathbf{m_i n_i V_{i\|} V_d \vec{b}_\perp} - \eta_{\|} \vec{b}\vec{b} \cdot \nabla V_{\mathrm{i}\|} - D_{\mathrm{i}} \vec{b}_\perp \vec{b}_\perp \cdot \nabla m_{\mathrm{i}} n_{\mathrm{i}} V_{\mathrm{i}\|} \Big) = -\vec{b} \cdot \nabla \mathrm{p} + S_{\mathrm{m}} \tag{2}$$

$$\nabla \cdot \left(\frac{5}{2} n_{\mathrm{e}} T_{\mathrm{e}} V_{\mathrm{i}\|} \vec{b} + \mathbf{\frac{5}{2} n_e T_e V_d \vec{b}_\perp} - \kappa_{\mathrm{e}} \vec{b}\vec{b} \cdot \nabla T_{\mathrm{e}} - \frac{5}{2} T_{\mathrm{e}} D_{\mathrm{i}} \vec{b}_\perp \vec{b}_\perp \cdot \nabla n_{\mathrm{e}} - \chi_{\mathrm{e}} n_{\mathrm{e}} \vec{b}_\perp \vec{b}_\perp \cdot \nabla T_{\mathrm{e}} \right) = -k(T_{\mathrm{e}} - T_{\mathrm{i}}) + S_{\mathrm{ee}} \tag{3}$$

$$\nabla \cdot \left(\frac{5}{2} n_{\mathrm{i}} T_{\mathrm{i}} V_{\mathrm{i}\|} \vec{b} + \mathbf{\frac{5}{2} n_i T_i V_d \vec{b}_\perp} - \kappa_{\mathrm{i}} \vec{b}\vec{b} \cdot \nabla T_{\mathrm{i}} - \frac{5}{2} T_{\mathrm{i}} D_{\mathrm{i}} \vec{b}_\perp \vec{b}_\perp \cdot \nabla n_{\mathrm{i}} - \chi_{\mathrm{i}} n_{\mathrm{i}} \vec{b}_\perp \vec{b}_\perp \cdot \nabla T_{\mathrm{i}} \right) = +k(T_{\mathrm{e}} - T_{\mathrm{i}}) + S_{\mathrm{ei}} \tag{4}$$

where V_{d} is the prescribed $E \times B$ drift velocity. Note 'prescribed drift' means the drift has to be predefined and read as input field in the code. This is applicable in our study, because the edge plasma potential is obtained from experiments and the associated $E \times B$ drifts are in their final steady state.

In cylindrical geometry, the same plasma and transport parameters are assumed in the code and in the analytical model. Plasma transport only in the perpendicular direction is considered. The particle and electron energy transport equations verified are:

$$\nabla \cdot (\mathrm{n_i V_d \vec{b}_\perp} - D_{\mathrm{i}} \vec{b}_\perp \vec{b}_\perp \cdot \nabla n_{\mathrm{i}}) = S_{\mathrm{p}} \tag{5}$$

$$\nabla \cdot \left(\frac{5}{2} \mathrm{n_e T_e V_d \vec{b}_\perp} - \chi_{\mathrm{e}} n_{\mathrm{e}} \vec{b}_\perp \vec{b}_\perp \cdot \nabla T_{\mathrm{e}} \right) = +S_{\mathrm{ee}} \tag{6}$$

In our verification study, the prescribed drift velocity is assumed as $\mathrm{V_d} = 40\ \sin^3(\rho_{\mathrm{pol}} - 0.965)\ \mathrm{m\ s^{-1}}$. Only one period of the sinusoidal is used and the rest part of $\mathrm{V_d}$ ($\rho_{\mathrm{pol}} < 0.93$ and $\rho_{\mathrm{pol}} > 1$) is assumed as zero. For the verification of mass equation (5), the ion density n_{i} is treated as the only variable while other parameters are assumed as constants. These include the electron temperature $T_{\mathrm{e}} = 50\,\mathrm{eV}$, the particle diffusion coefficient $D = 0.75\ \mathrm{m^2\ s^{-1}}$ and the particle source term $S_{\mathrm{p}} = 20\,\mathrm{m^{-2}\,s^{-1}}$. For the verification of energy equation (6), the electron temperature T_{e} is the only variable. The other constant parameters are the electron density $n_{\mathrm{e}} = 1.0 \times 10^{19}\ \mathrm{m^{-3}}$, the heat transport coefficient $\chi = 1.5\ \mathrm{m^2\ s^{-1}}$ and the energy source term $S_{\mathrm{ee}} = 8$ KW. Good agreement between the code results and the analytical model (see figure 2) confirms the drifts added in the code are reasonable.

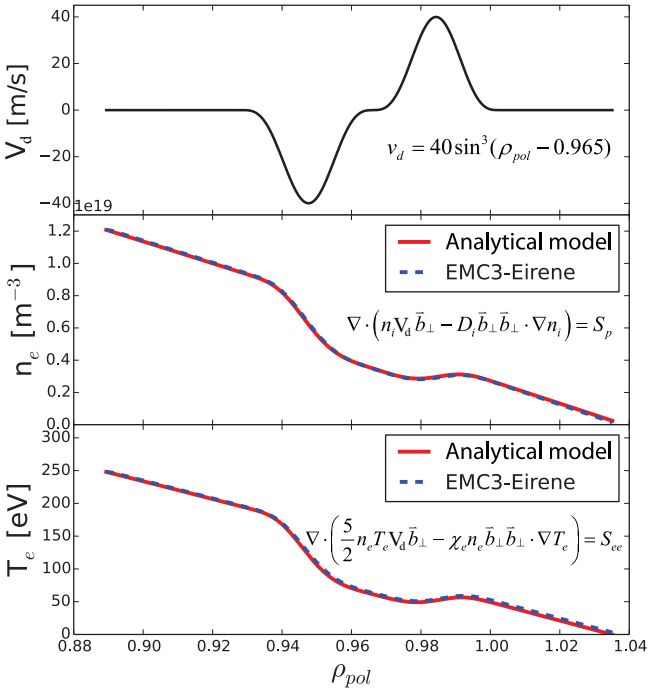

Figure 2. Verification of the particle and energy transport equations including the prescribed drift terms.

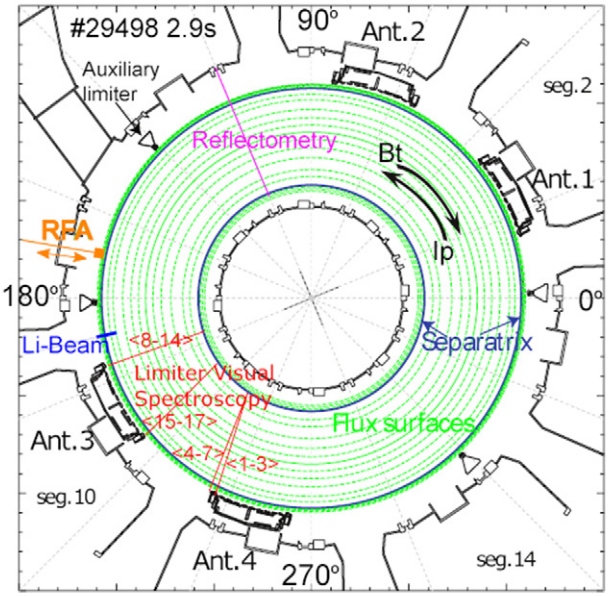

Figure 3. Top view of AUG shows the toroidal positions of the ICRF antennas, limiters and the main diagnostics.

3. Experimental results

Firstly experimental evidences of the ICRF induced SOL modification are discussed. The toroidal positions of the

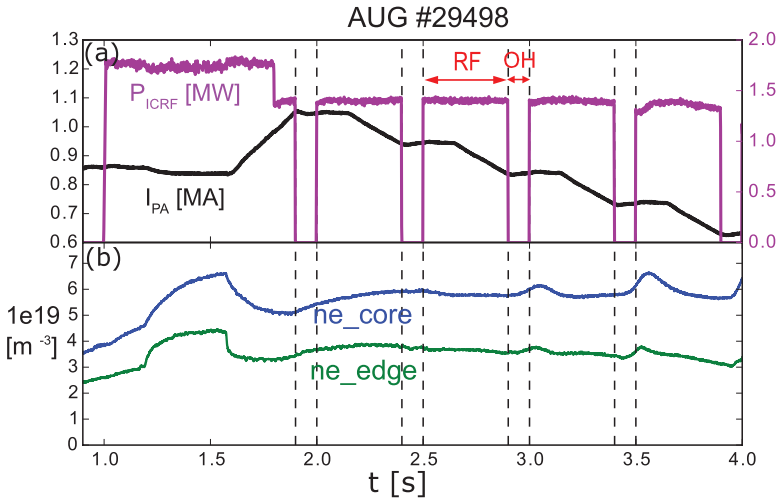

Figure 4. Plasma parameters as a function of time. (a) Plasma current and ICRF power; (b) the core and edge plasma density.

ICRF antennas, limiters and diagnostics are illustrated in the top view of AUG (figure 3). The whole torus is divided into 16 sectors and 0° is set at the boundary of sector 1 and 16. The discharge of consideration is #29498, a typical AUG L-mode with $B_0 = -2.0$ T, $I_0 = 1$ MA, $P_{\text{total}} \sim 1.83$ MW, $f_{\text{ICRF}} = 30$ MHz, $ne_{\text{core}} \sim 6.0 \times 10^{19}$ m^{-3} and $ne_{\text{edge}} \sim 3.0 \times 10^{19}$ m^{-3}. The ohmic heating (OH) and the ICRF heating are switched on in turn to provide the same amount of total heating power. During the ICRF heating, antennas 2 and 4 are powered in pair to provide the total auxiliary heating power for a standard D (H) minority scenario. Both antennas are 2-strap antennas with toroidal π phasing. Here we use the OH and RF phases to represent the time periods during the OH and ICRF heating, respectively. The influence of ICRF on edge plasma can be inferred through the comparisons of the plasma parameters during these two phases. The whole discharge is formed in a way with several steady state values of plasma current (figure 4). The magnitude of the current in each 'step of plasma current' is different. This is to generate plasma equilibriums with different q_{95}, so that diagnostics such as the reciprocating retarding field analyzer (RFA) near the antennas can be magnetically connected to different poloidal positions of the ICRF antenna (figure 5).

In AUG the SOL perturbations propagate for several meters along the magnetic field, the RF convection is suspected and the effect of the ponderomotive force is unlikely [5]. Thus, the density modifications in front of the powered antenna 2 can be analyzed by diagnostics magnetically connected to it. For this, field line tracings are made starting from the reflectometry, the RFA probe and the Li-beam (figure 5). The equilibriums used for field line tracings have different q_{95} values and is chosen from different 'step of plasma current', i.e. equilibriums at $t = 2.05$ s, 2.55 s, 3.05 s, 3.55 s, 4.05 s. The measurements are magnetically connected to different poloidal positions of the powered antenna, this allow us to reconstruct 2D profiles (poloidal and radial) instead of 1D. As shown in figure 6, the 2D mapping of the density from the reflectometry measurement is plotted versus coordinates of the connection point from the reflectometry to the left ICRF limiter of antenna 2. The density is averaged for time periods at (1.9, 2.0 s), (2.4, 2.5 s), (2.9, 3.0 s), (3.4, 3.5 s), (3.9, 4.0 s) for the OH phase, and (2.0, 2.15 s), (2.5, 2.65 s), (3.0, 3.15 s), (3.5, 3.65 s), (4.0, 4.1 s) for the RF phase. During the OH phase, the poloidal density ($\langle n_e \rangle_{\text{OH}}$) is largely homogenous from $Z = -0.03$ m to $Z = -0.11$ m. In comparison, the poloidal density during RF phase ($\langle n_e \rangle_{\text{RF}}$) is significantly modified (figure 6). $E \times B$ plasma flow from the region near $Z = -0.08$ m to $Z = -0.03$ m is suspected. To eliminate the effects of equilibrium on density, we have subtracted the density during the OH phase from the one during the RF phase, i.e. $\langle n_e \rangle_{\text{RF}} - \langle n_e \rangle_{\text{OH}}$. The results (figure 7) clearly show a density depletion from $Z = -0.10$ m to $Z = -0.07$ m and a density increase from $Z = -0.06$ m to $Z = -0.03$ m. Besides the density measurements, the RFA probe is also used to investigate the SOL modifications. Two quantities are measured with this probe: the mean parallel energy of the collected ions ($\langle W_{\parallel} \rangle_t$) and the saturated current on the slit (I_{slit}) [5]. Discussions about the relationship between

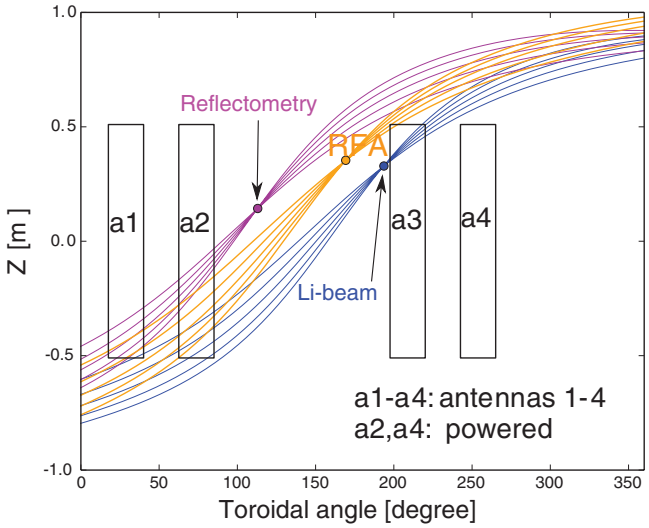

Figure 5. Magnetic field line tracings start from the Li-beam, reflectometry and RFA diagnostics. These measurements are magnetically connected to antenna 2. The equilibriums chosen for field line tracings are at time points of $t = 2.05$ s, 2.55 s, 3.05 s, 3.55 s, 4.05 s.

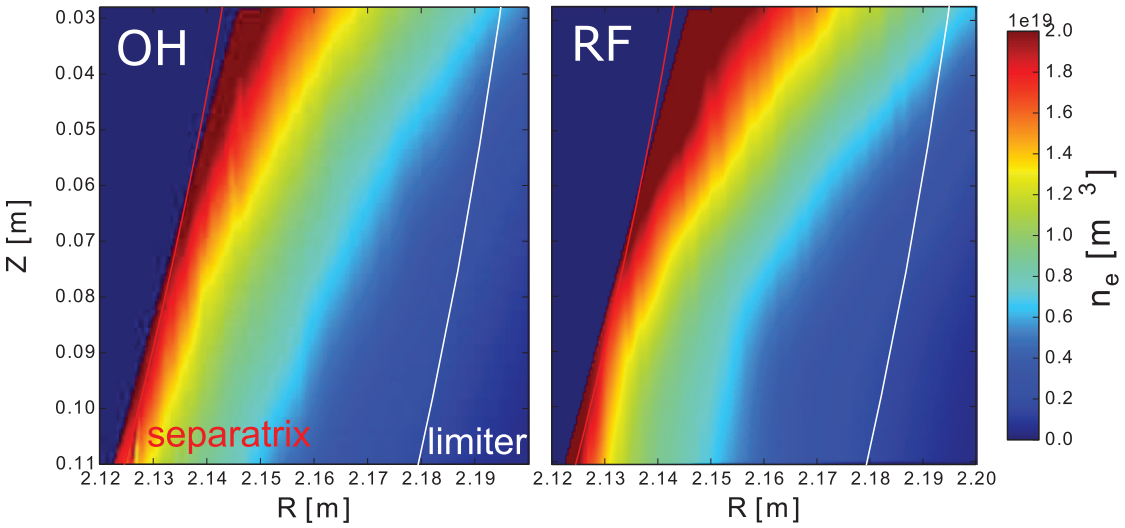

Figure 6. 2D mapping for the reflectometry measured electron density versus coordinates of the connection point from the reflectometry to antenna 2.

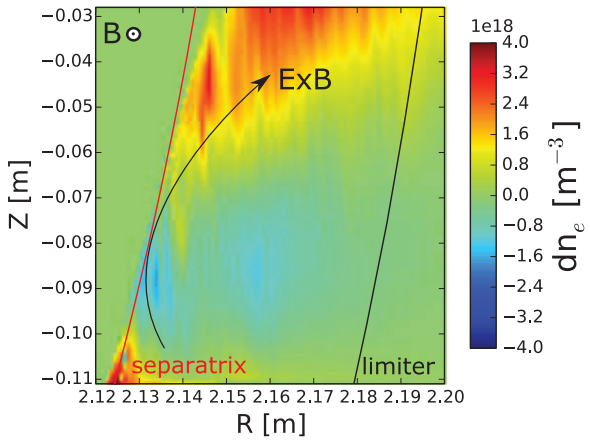

Figure 7. Density differences between the RF and OH phase. This is done by subtracting the density in figure 6(a) from the one in figure 6(b), i.e. $\langle n_e \rangle_{\mathrm{RF}} - \langle n_e \rangle_{\mathrm{OH}}$.

$\langle W_{\parallel} \rangle_t$ and the potential are given in section 4.2. By moving the RFA probe radially one can get a radial $\langle W_{\parallel} \rangle_t$ profile in front of antenna 2; by changing I_{p} and q_{95}, the RFA is magnetically connected to different poloidal positions. Thus the 2D $\langle W_{\parallel} \rangle_t$ and I_{slit} profiles (see figures 11(a) and 15(a)) in the lower part of antenna 2 can be derived. The results indicate that zones of local plasma biasing are formed via sheath rectification, and density convection is thus created due to the spatial inhomogeneous of the biased potential. Therefore, the RF convection plays an important role in driving plasmas from the lower part of figure 7 to the upper part.

4. Simulation results

Simulations are carried out along the following steps: (a) Reconstructing plasma transport parameters from measurements to achieve realistic background plasma; (b) Applying the experimental data from the RFA probe and calculating the 3D potential and $E \times B$ drifts; (c) Modelling the density modifications induced by RF convection; (d) Calculating the particle and power fluxes to the wall. The detailed simulation flow chart is shown in figure 8.

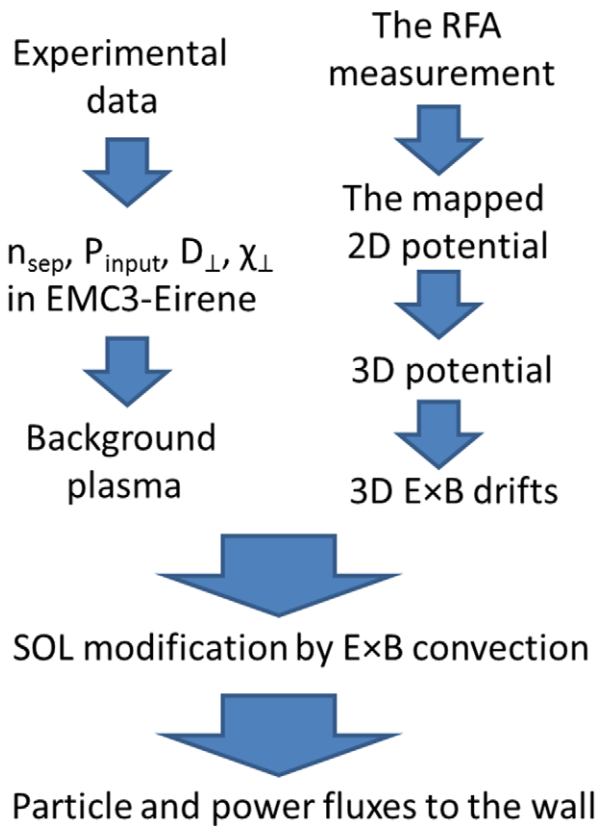

Figure 8. The simulation flow chart.

4.1. Background plasma

As discussed in the introduction, the spatial structures of the magnetic field lines are critically important in our study and

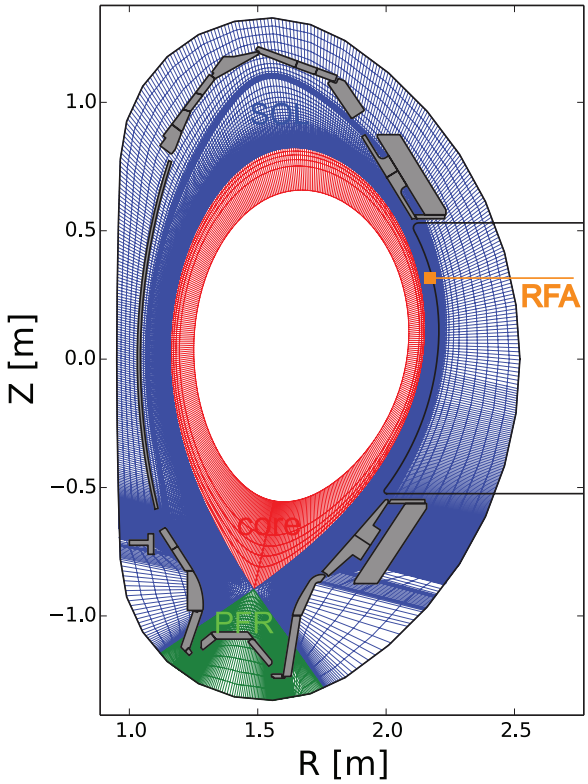

Figure 9. Poloidal cross-section of the computational grid at $\phi = 0°$.

no toroidal symmetry can be assumed. Thus, we have built a toroidal 360° computation grid based on the equilibrium from #29498 at 2.92 s. The whole computational grid is composed of sixteen equally constructed segments. Each segment represents one sector of the torus (figure 3), and is divided into the core, SOL and PFR (private flux region) (figure 9). The SOL region of the computation grid is extended to the wall to accomplish two goals: firstly the plasma density right in front of the ICRF antennas can be calculated; secondly the recycling flux from the main chamber wall can be taken into account. Compared to the previous 360° EMC3-Eirene computation grid [29], we have increased the grid resolution in the far SOL, so that the calculations of drifts near the antennas can be more accurate. We include in the integration domain the eight ICRF limiters, four auxiliary limiters, the inner heat shield and the lower and upper divertors.

As the first step the simulations for the OH phase are carried out to generate the background plasma for the RF phase. For this, experimental measurements during the OH phase (at $t = 2.95$ s) is used to reconstruct the background plasma in simulations. In our simulations no impurity is considered. The total input power in our simulation is set as $P_{\text{total}} = 1.3$ MW, which equals to the total heating power minus the radiated power. The separatrix density is set as $n_{e\_\text{sep}} = 2.0 \times 10^{19}\ \text{m}^{-3}$ and is used as a boundary condition. By choosing the proper plasma transport parameters, i.e. the particle and heat diffusion coefficients $D_\perp$ and $\chi_\perp$ ($\chi_{\perp_e}$ is assumed to be equal to $\chi_{\perp_i}$), the upstream and downstream profiles in the SOL are best fitted to the experimental data (figure 10). The profiles validated against experiments include the density and temperature in the mid-plane and the particle and power fluxes to the divertor outer target. The experimental diagnostics used in the validation include the Li-beam, the edge and core Thomson scattering, the divertor probes and the infrared camera.

4.2. 3D potential

When assuming mono-energetic ions at sheath entrance, the averaged parallel energy $\langle W_\parallel \rangle_t$ measured with the RFA is equal to the Bohm energy plus the time-averaged (DC) sheath potential [30], i.e. $\langle W_\parallel(t) \rangle = \langle M_i u_{\text{Bohm}}^2/2 \rangle + \langle eV_{\text{sh}}(t) \rangle$, in which u_{Bohm} is the ion sound speed. $\langle M_i u_{\text{Bohm}}^2/2 \rangle$ is the energy gained in the pre-sheath and $\langle eV_{\text{sh}}(t) \rangle$ is the one gained in the sheath. Thus, the whole plasma potential (Φ_{pl}) which equals to the potential drop in the pre-sheath and sheath (Φ_{pre} and Φ_{sh}) can be calculated with $\Phi_{\text{pl}} = \Phi_{\text{pre}} + \Phi_{\text{sh}} = (\langle W_\parallel \rangle_t)/q$. Here we use Φ_{RF} to represent Φ_{pl} in the presence of powered antenna. Since Φ_{RF} is nearly constant along the magnetic field, its value in other toroidal positions can be extrapolated by tracing magnetic field lines. As shown in figure 11(a), $\langle W_\parallel \rangle_t$ is plotted versus the (R, Z) coordinates in front of antenna 2 (toroidal angle $\phi = 74.53°$). The lower part of antenna 2 is magnetically connected to the RFA. During the field line tracings, magnetic field lines are assumed to be continuous even though a small part of them are interrupted by the limiters. In reality, Φ_{RF} in the private region of the powered antenna (a region between the two side ICRF limiters) is different from that in the outer side of the limiter. We have made this assumption because Φ_{RF} in the private region of the antennas cannot be measured with the present diagnostics.

As indicated from the RFA measurements (figure 11(a)), one of the most obvious features of the RF sheath rectification is the formation of the perturbed 'potential blobs'. Three Φ_{RF} blobs ($\Phi_{\text{RF\_A}}$, $\Phi_{\text{RF\_B}}$, $\Phi_{\text{RF\_C}}$) in the lower part of antenna 2 can be pointed out. The Φ_{RF} in the unperturbed region is quantitative below 50 V, while Φ_{RF} in the perturbed region can reach 180 V. In order to eliminate the effect due to data noises, we have applied a Gaussian potential to fit the experimental Φ_{RF}. The Gaussian potential Φ_{G} used in the fitting has the form:

$$\Phi_{\text{G}} = \Phi_0 \cdot \exp\left\{ -\left[\frac{(R - R_0)^2}{2\sigma_R^2} + \frac{(Z - Z_0)^2}{2\sigma_Z^2} \right] \right\} \qquad (7)$$

Here, (R_0, Z_0) and Φ_0 are the coordinate and potential value of the center point of the Φ_{RF} blob, σ_R and σ_Z are the standard deviations of Φ_{G} in the radial and vertical directions, respectively. An example of fitting Φ_{RF} with Φ_{G} for potential blob B is illustrated in figure 12. Firstly a series of scans both in the radial and vertical directions are made to figure out the central point of the potential blob and the maximum potential (Φ_0) value, thus $\Phi_0 = 182.5$ V and (R_0, Z_0) = (2.07 m, −0.38 m) are obtained. By fixing Z at Z_0 or R at R_0 and let Φ_{G} varying as a function of R or Z, one can get $\sigma_R = 0.013$ and $\sigma_Z = 0.042$, respectively. With the same principle, the parameters obtained for Φ_{RFA} are: $\Phi_0 = 80$, (R_0, Z_0) = (2.107 m, −0.3 m), $\sigma_R = 0.008$, $\sigma_Z = 0.065$; those for $\Phi_{\text{RF\_C}}$ are: $\Phi_0 = 160$,

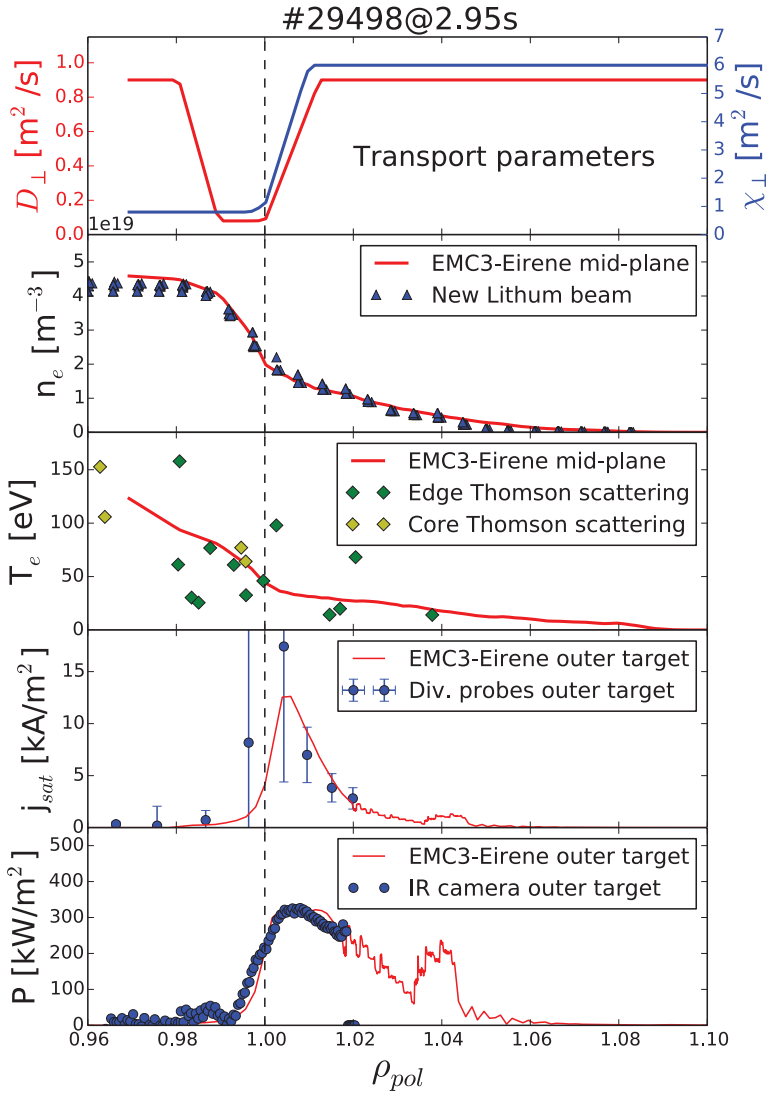

Figure 10. The SOL parameters in the code are best fitted to the experimental data. These include the mid-plane density and temperature profiles, the particle and power fluxes to the divertor outer target.

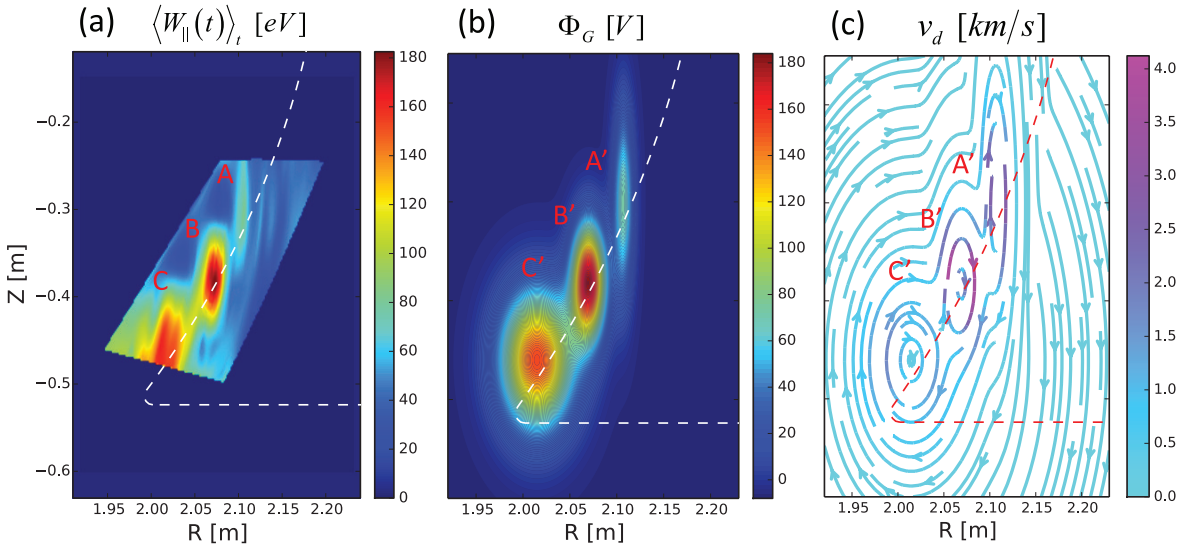

Figure 11. (a) The parallel ion energy versus (R, Z) coordinate in the middle of antenna 2, reproduced with permission from [5]. Copyright 2014 AIP Publishing LLC. (b) The Gaussian potential based on the experimental potential calculated from (a). (c) The drift velocities of (b).

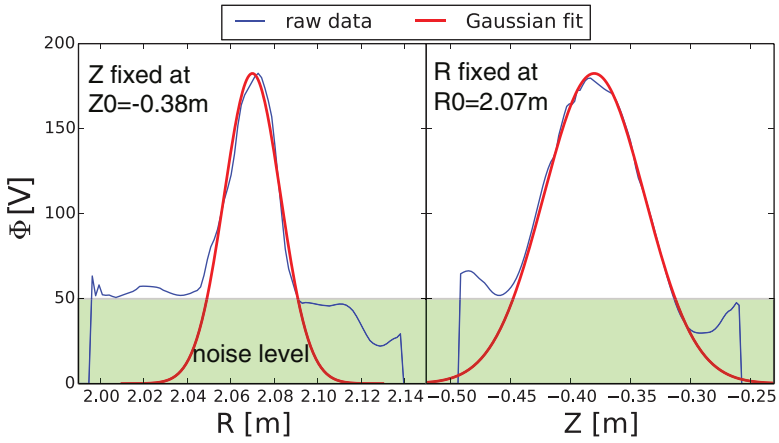

Figure 12. Comparisons of the Gaussian fit with the raw data for the potential blob B. (R_0, Z_0) are the coordinates of the center point of the potential blob.

$(R_0, Z_0) = (2.015\ \text{m}, -0.46\ \text{m})$, $\sigma_R = 0.025$, $\sigma_Z = 0.05$. Note Φ_{RF} in the upper part of the antenna is unknown in experiments, thus we only consider the density modifications in the lower part of antenna 2.

Then we start to extrapolate the 2D Φ_{G} into 3D with the assumption that Φ_{G} is constant along the magnetic field. An example of 3D extrapolations of Φ_{G} is shown in figure 13. The start points for field line tracings are chosen in the middle of antenna 2 ($\phi = 74.53°$) and they are selected to have high resolution.

After obtaining the 3D potential, the drift velocities are then calculated with the formula

$$\vec{v}_{\text{d}} = (\vec{E} \times \vec{B})/B^2 = \Big[(E_Z B_\phi - E_\phi B_Z)\vec{R} + (-E_R B_\phi + E_\phi B_R)\vec{Z} + (E_R B_Z - E_Z B_R)\vec{\phi}\Big]/B^2 \tag{8}$$

Note ϕ here represents the toroidal direction. Since $B_\phi \gg B_R$, R_Z and $E_\phi \ll E_R$, E_Z, thus only the radial and vertical (R and Z, respectively) components of the drift velocity are important. If we neglect the significant smaller terms, the drift velocity then has the form

$$\vec{v}_{\text{d}} = \left(-\nabla_Z \Phi \cdot B_\phi \vec{R} + \nabla_R \Phi \cdot B_\phi \vec{Z}\right)/B^2 \tag{9}$$

Note the two components of the drift v_R and v_Z are calculated separately and are read as two input fields in the code. Figure 11(c) shows the drift velocities calculated based on the potential in figure 11(b). The magnitude of the drift velocities are denoted with the color and the directions of them are depicted with the arrows. Since the drift velocities are calculated based on the gradient of the potential, their structures are similar to the associated potential contours. Plasma flows from one convective cell to another one can be pointed out where convective cells overlap. The vertical component of the drift velocity is in the range of 10^3 m s^{-1}, while the radial component is in the range of 10^2 m s^{-1}. This is because the potential gradient in the radial direction is much larger than the one in the vertical direction. In addition the vertical component of the drift velocity is not parallel to the antenna, thus it can play a more important role than the radial component in driving plasma flows to the wall.

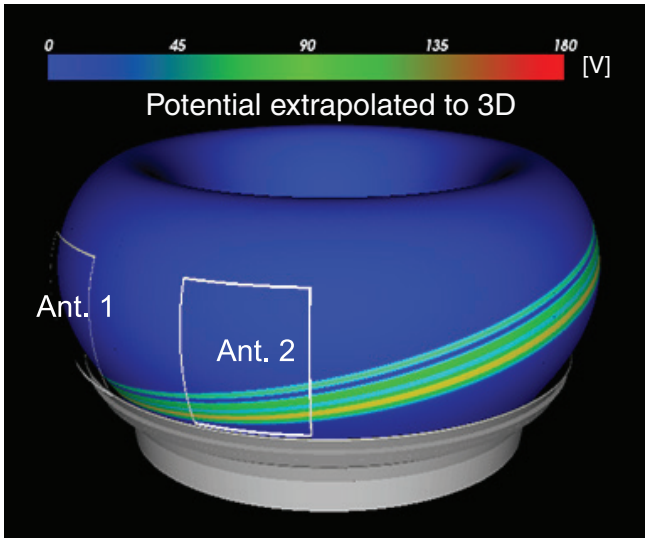

Figure 13. Extrapolations of the 2D potential in figure 11(b) to 3D with the field line tracing technique.

4.3. Density modifications by RF convection

To investigate the SOL modifications during the RF phase, the convective $E \times B$ drifts are then superimposed onto the background plasma (figure 8). This is done by using the background plasma as initial plasma conditions, reading the prescribed $E \times B$ drifts and performing new iterations with the new version of EMC3-Eirene which solves equations (1)–(4). Note that in our simulations, drifts are only considered where the potential value is larger than 50 V. This is because during the OH phase $\langle W_\parallel(t)\rangle_t$ remains everywhere below 50 eV, while during the RF phase $\langle W_\parallel(t)\rangle_t$ is quantitatively larger than 50 eV in the perturbed zone. The potentials in the OH phases are described solely by plasma temperature, whereas in the RF phases they are described both by the temperature and the rectified sheath potentials. It is the perturbed zones where the convective cells formed that are of interest to us. Moreover, as indicated in figure 12, the potential noise in the unperturbed zones ($\Phi_{\text{RF}} < 50$ V) is relative large and can cause undesired chaotic $E \times B$ drifts.

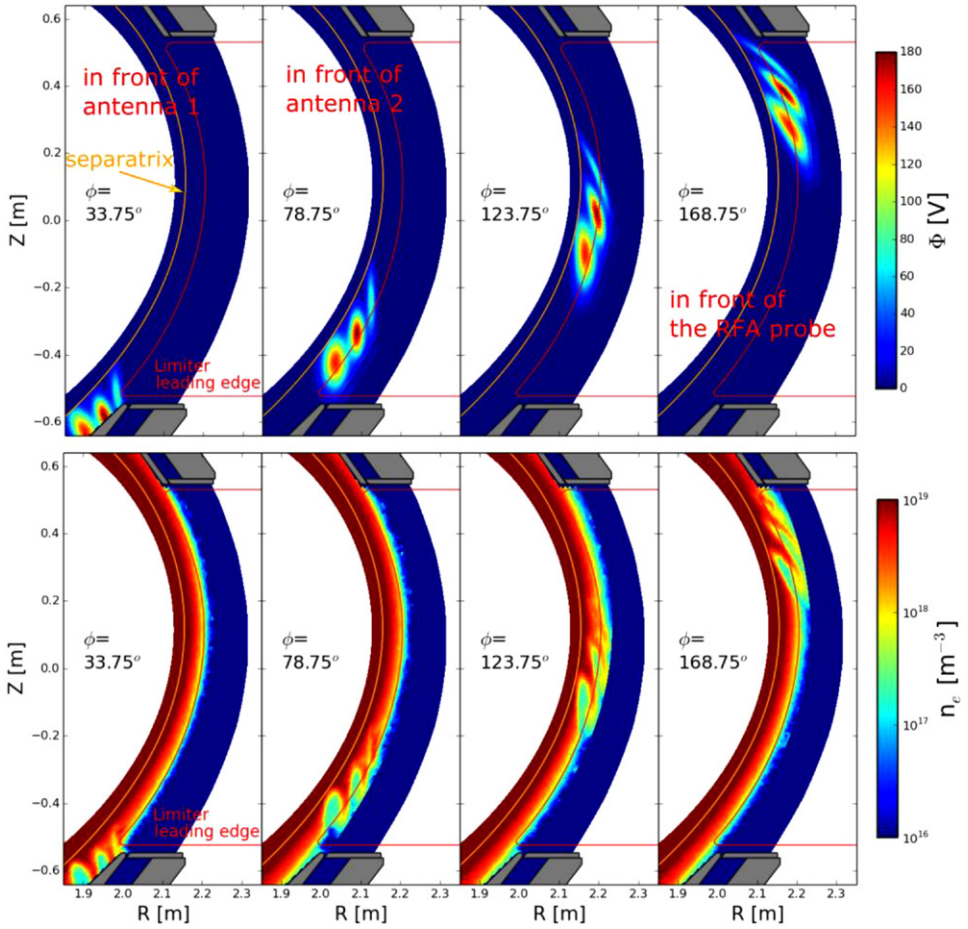

Figure 14. The plasma potential (top) and density modifications (bottom) in different toroidal positions.

After the numerical iterations, i.e. when the plasma reaches a new steady state, the ICRF induced SOL modifications are obtained. In order to understand how the SOL density is changed, the electron density and the associated potential in different toroidal positions are shown in figure 14. The convective cells have the same outlines with the potential blobs. They extend from the antennas to the separatrix with their centers located near the leading edge of the limiter. The convective $E \times B$ drifts drive plasma flows locally and induce poloidal inhomogeneous density in the SOL. Density depletions are seen within the domains of convective cells, while density increases are observed in the peripheries of the convective cells where the convective flows intersect with the wall. These local density depletions due to the RF convection are also known as the 'density pump-out' effects. As a global effect, the convective cells tend to drive the plasma outwards, flatten the density profiles in the perturbed regions and broaden the SOL. Moreover, as more plasma fluxes are driven to the wall, the strength of the plasma-wall interactions is enhanced.

Because the RF rectified potential is constant along the magnetic field, the convective cells tend to propagate along magnetic field lines, i.e. the convective cells are 'frozen' in the flux tubes. Consequently the flux tubes act as the 'media' and the density perturbations also propagate along magnetic field lines in the toroidal direction. From this point of view, the powered ICRF antenna acts as a giant biased probe and perturbs the SOL densities in flux tubes which pass in front of it. The $E \times B$ drifts induced density perturbations travel from the powered antenna to the RFA probe while keeping the similar convection structures (figure 14). The distortion of the convection structures in the toroidal direction is due to the twist of the flux tubes. It is found that the local density perturbations can propagate at least several meters in AUG, but to which extend still requires further experimental investigations. In Tore Supra the average effects of RF potentials are indicated to be able to propagate 12 m along magnetic field lines [31].

For the discharges considered in the paper, since no Neutral Beam Injection heating is used, thus the particle sources are from the recycling flux and the injected fueling gas. About 96% of the total recycling flux comes from the divertor while the part generated at the limiters only accounts for ~2%. The ICRF induced $E \times B$ drifts can however locally increase the recycling flux from the limiters by ~28%. Thus the total particle sources during the OH and RF phases are almost same, but during the RF phase the particle flux from the wall is locally (in the convective cell regions) increased.

Our simulated density is in qualitative agreement with the experiments. This is illustrated in figure 15 which shows the comparisons of the normalized ion saturation current (I_{slit}) from the RFA measurements, the simulated ion saturation current (I_{sat}) and electron density in front of antenna 2

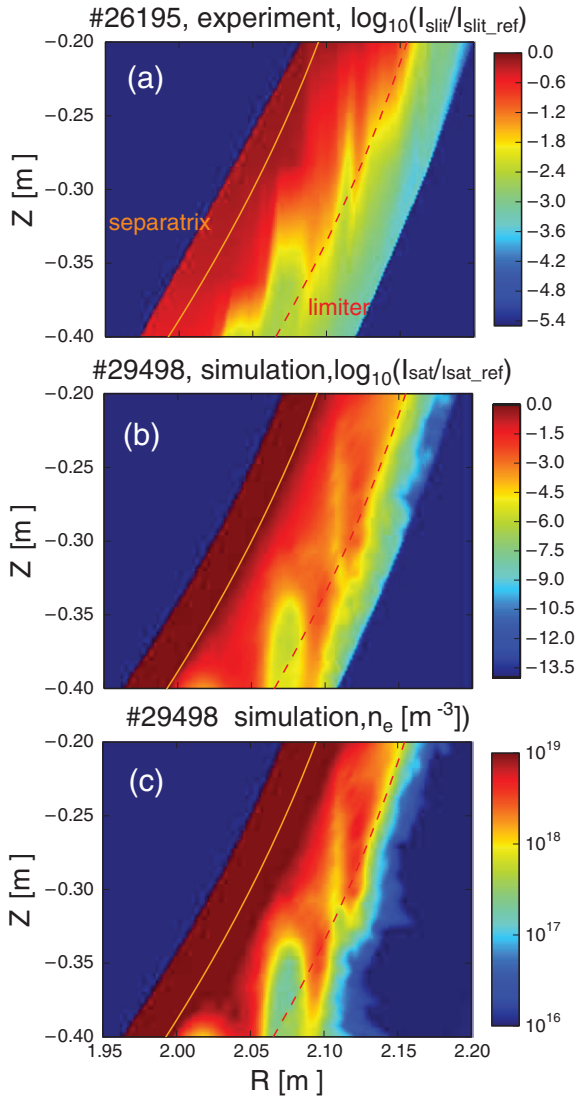

Figure 15. Comparison between experiment and simulation. (a) Normalized slit current in experiment. (b) Normalized ion saturation current in simulation. (c) Electron density in simulation.

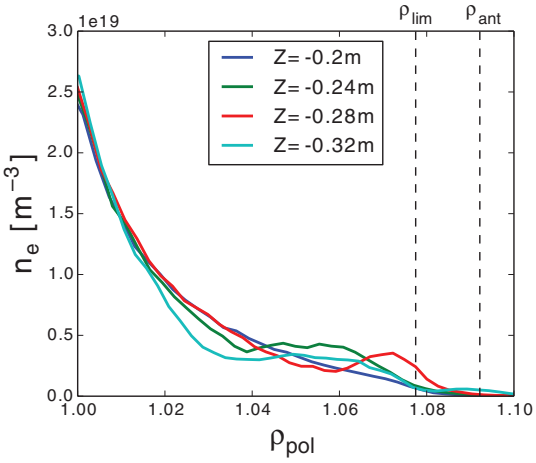

Figure 16. Radial density scans at different vertical positions. $\rho_{\rm lim}$ and $\rho_{\rm ant}$ are the radial positions of the limiter and ICRF antenna, respectively.

($\phi = 74.53°$). The ion saturation current in simulations is calculated with the formula $I_{\rm sat} = qn_{\rm e}C_{\rm s}$, in which $C_{\rm s}$ is the plasma sound speed. The two shots #26195 and #29498 have the same ICRF heating power and nearly the same plasma parameters. In experiment, $I_{\rm slit}$ is normalized to its average value over 2.155 m $< R_{\rm RFA} <$ 2.161 m. The same normalization procedure is done for the simulated $I_{\rm sat}$. The $I_{\rm sat}$ value ~3 cm in front of the limiter is used as a reference ($I_{\rm sat\_ref}$). Good agreement is found between the measured (figure 15(a)) and simulated (figure 15(b)) ion saturation current, in particular the same 'density pump-out' structures are well reproduced in the simulations. Some differences can also be pointed out, such as the intensity the normalized ion saturation current. One possible reason for this difference is that for the calculations of the experimental ion saturation current, the collection area of the RFA slit is somehow underestimated. Moreover the formulas for the ion saturation current are based on assumptions that may not be fully satisfied. They originate from 1D reasoning omitting effects of the actual geometry. Effects such as particles able to stream around an object cannot be captured by a formula that looks at things in 1 dimension. Aside from that there are error bars on the quantities needed to evaluate the saturation current, such as the ion and electron temperatures.

Furthermore, density scans are made for the modified density (figure 15(c)) at vertical positions of $Z = -0.2$ m, -0.24 m, -0.28 m, -0.32 m, respectively (figure 16). The density profile at $Z = -0.2$ m is not influenced by the convective drifts and is used as a reference. During the OH phase, the poloidal density is homogenous and the density profiles in different vertical positions are the same as the one at $Z = -0.2$ m. During the RF phases, density profiles within the domain of the convective cells are substantially modified, such as the ones at $Z = -0.24$ m, -0.28 m, -0.32 m, as shown in figure 16. Pump-out effects can also be inferred from these 1D profiles: density depletions are seen where the convective cell is located, while density increases are seen in the outer positions.

The change of density in front of the antenna influences the ICRF power coupling. The coupling of ICRF power decreases exponentially as the evanescent distance (from the antenna to the cut-off density (~0.4×10^{19} m^{-3})) of the fast wave increases. In our simulations only part of the density redistributions in front of the antennas are known, thus it is hard to conclude whether the total power coupling is increased or decreased. For quantitative calculations of the coupling resistance, the whole density and temperature redistribution in front of the antenna need to be known. This necessitates the correct description of the potential covering the whole range of the powered antenna, which is considered in our future work.

4.4. Plasma-wall interactions

As described before, the RF convection can significantly increase the local plasma flows to the wall and enhance the intensity of plasma-wall interactions. The particle and power fluxes to the wall (j and P) can be calculated with the formulas $j = nv$ and $P_{\parallel} = \gamma n_{\rm t} k T_{\rm t} c_{\rm s}$ respectively, in which $\gamma \approx 7$ is the sheath heat transmission coefficient and $c_{\rm s}$ is the plasma sound

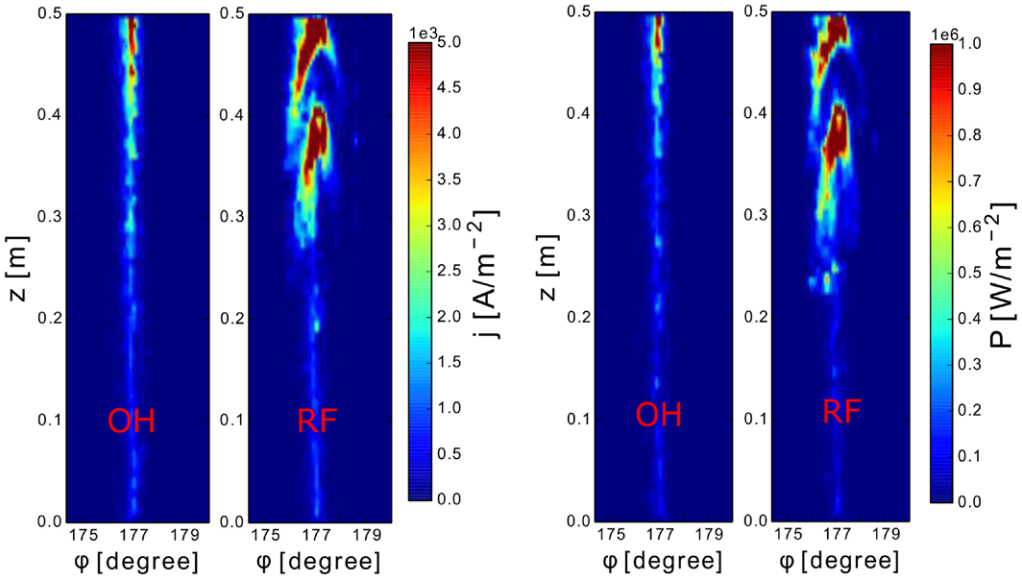

Figure 17. Comparisons of the particle and power fluxes to the auxiliary limiter 3 during the OH phase and the RF phase.

velocity [32]. An example is shown in figure 17, which depicts the calculated j and P for the upper part of auxiliary limiter 3 (the limiter nearest to the RFA probe). The results indicate that the intensity of j and P as well as the plasma 'wetted' area are significantly increased during the RF phase. For instance, the maximum power density load on the limiter during the RF phase is about 3 times as large as the one during the OH phase. The observed j and P on the limiter are consistent with the convective plasma flows in front of it. They are significantly increased where the convective plasma flows intersect with the limiter. Because the convective drifts are local effects, the enhancement of power load on the limiter due to these convective drifts is also local. Excessive heat loads can be imposed on the plasma facing components which are magnetically connected to the powered antenna. As a result, these plasma facing components have a much higher probability of being damaged.

5. Conclusions and outlooks

For the first time ICRF induced edge plasma density convection in realistic 3D geometry is simulated with the 3D code EMC3-Eirene in AUG. For this we have added the prescribed drift terms into the EMC3 equations and verified them in the code. Our simulation results are in qualitative agreement with the experiments, which indicate the differential biased edge plasma potential due to sheath rectification is the source of convective $E \times B$ drifts. The $E \times B$ drifts can induce steady state convective cells and cause poloidal inhomogeneous density in front of the antenna. Density depletions are seen within the convective cells while density increases are observed where the convective flows intersect with the wall. Moreover, the convective cells and the local density perturbations are able to propagate several meters along magnetic field lines. It is found that the RF convection can significantly increase the local plasma flows to the wall, influence the ICRF coupling, broaden the SOL and enhance the strength of plasma-wall interactions.

Furthermore, we plan to carry out comprehensive simulations by running the EMC3-Eirene and SSWICH [33] code in an iterative and quasi self-consistent way. The simulations will be performed for the 2-strap and 3-strap antennas both in L and H modes. An integrated and comprehensive description of the ICRF induced SOL modifications is foreseen.

Acknowledgments

This work has been carried out within the framework of the EUROfusion Consortium and has received funding from the Euratom research and training programme 2014–2018 under grant agreement No. 633053. The views and opinions expressed herein do not necessarily reflect those of the European Commission.

References

[1] Stix T H 1992 *Waves in Plasmas* (New York: American Institute of Physics)
[2] Myra J R *et al* 1994 *Phys. Plasmas* **1** 2890–900
[3] D'Ipoolito D A *et al* 2008 *Phys. Plasmas* **15** 102501
[4] D'Ippolito D A *et al* 2006 *Phys. Plasmas* **13** 102508
[5] Colas L *et al* 2014 2-Dimensional mapping of ICRF-induced scrape-off layer modifications with a retarding field analyser on ASDEX-Upgrade *20th Topical Conf. on Radio Frequency Power in Plasmas (Sorrento, Italy, 2013)* vol 1580 pp 259–62
[6] Bobkov V *et al* 2010 *Nucl. Fusion* **50** 035004
[7] Colas L *et al* 2015 *J. Nucl. Mater.* **463** 735–8
[8] Qin C M *et al* 2013 *Plasma Phys. Control. Fusion* **55** 015004
[9] Colas L *et al* 2007 *J. Nucl. Mater.* **363** 555–9
[10] Ochoukov R *et al* 2014 *Plasma Phys. Control. Fusion* **56** 015004
[11] D'Ippolito D A *et al* 1993 *Phys. Fluids* B **5** 3603–17
[12] Dux R *et al* 2007 *J. Nucl. Mater.* **363** 112–6
[13] D'Ippolito D A *et al* 1998 *Nucl. Fusion* **38** 1543–63
[14] Noterdaeme J M *et al* 1993 *Plasma Phys. Control. Fusion* **35** 1481–511

[15] Myra J R *et al* 2006 *Nucl. Fusion* **46** S455–68
[16] Butler H S *et al* 1963 *Phys. Fluids* **6** 1346–55
[17] Lieberman M A 1988 *IEEE Trans. Plasma Sci.* **16** 638–44
[18] Becoulet M *et al* 2002 *Phys. Plasmas* **9** 2619–32
[19] D'Ippolito D A *et al* 1991 *Plasma Phys. Control. Fusion* **33** 607–42
[20] D'Ippolito D A *et al* 2011 *J. Nucl. Mater.* **415** S1001–4
[21] Myra J R *et al* 1990 *Nucl. Fusion* **30** 845–58
[22] Bobkov V *et al* 2011 *J. Nucl. Mater.* **415** S1005–8
[23] Lau C *et al* 2013 *Plasma Phys. Control. Fusion* **55** 095003
[24] Feng Y *et al* 2004 *Contrib. Plasma Phys.* **44** 57–69
[25] Van Eester D *et al* 2013 *Plasma Phys. Control. Fusion* **55** 025002
[26] Van Eester D *et al* 2015 *Phys. Plasmas* **22** 122505
[27] Feng Y *et al* 2014 *Contrib. Plasma Phys.* **54** 426–31
[28] Reiter D *et al* 2005 *Fusion Sci. Technol.* **47** 172–86
[29] Zhang W *et al* 2016 *Nucl. Fusion* **56** 036007
[30] Soucek J *et al* 2005 *J. Geophys. Res. Space Phys.* **110**
[31] Kubic M *et al* 2013 *J. Nucl. Mater.* **438** S509–12
[32] Stangeby P C 2000 *The Plasma Boundary of Magnetic Fusion Devices* (Bristol: Institute of Physics Publishing)
[33] Jacquot J *et al* 2014 *Phys. Plasmas* **21** 061509